AM-AFM Systems Analysis and Output Feedback Control Design with Sensor Saturation

Yongchun Fang, *Senior Member, IEEE*, Yudong Zhang, Ningning Qi, and Xiaokun Dong

***Abstract*—This paper analyzes the dynamics of an amplitude modulation atomic force microscopy (AM-AFM) system, and designs a novel output feedback robust adaptive control (OFRAC) law to improve the scanning performance of the AM-AFM system. That is, a control-oriented reduced model is proposed to approximate the mapping from tip-sample separation to oscillation amplitude, whose accuracy is verified by experimental results. Considering the facts that the parameters of an AM-AFM system vary with different combinations of piezo-scanner and cantilever as well as detected samples, and measurement saturation occurs frequently in dynamic AFM systems, an OFRAC strategy for the piezo-scanner is designed to keep the oscillation amplitude of the cantilever staying at the desired set-point under various complex situation. It is shown theoretically that the proposed control strategy pushes the system away from the saturation state in finite time, and it ensures uniform ultimate boundedness (UUB) result for the control error. The OFRAC strategy is applied to a virtual AM-AFM system, and the collected results clearly demonstrate that it presents superior imaging performance for high-speed scanning tasks.**

***Index Terms*—Atomic Force Microscopy, Saturation, Output Feedback Control, Robust Adaptive Control, Lyapunov Techniques.**

I. INTRODUCTION

SINCE its invention [1], an atomic force microscopy (AFM) has been widely utilized in nano-science and nano-technology field. With the help of an AFM, we can characterize the micro-world in nanometer scale [2], [3], or even manipulate a single atom [4]. Subsequently, to reach atomic resolution and to reduce the damage to probes or samples, researchers have proposed the scheme of dynamic AFMs in which the probe is excited by a sinusoidal signal. Later on, the emergence of the amplitude modulation AFM (AM-AFM) [5], which is also called as "tapping mode", enhances the performance of dynamic AFMs remarkably. However, with the rapid development of nano-technology, current AFMs can not meet the daily-increasing requirements in various research areas including life science, material engineering, and so on.

The basic principle of dynamic AFMs is to regulate the extended or contracted displacement of a piezo-scanner to keep the separation between the measured sample and the probe tip staying at the setpoint [6]. From the view point of control, this is a typical error-based control system [7]. In conventional AFM systems, the classical proportional-integral (PI) controller is often employed to adjust the position of the sample to obtain the topography data. As generally known, the PI control law presents such advantages as no requirements for plant model, easy implementation in digital control systems, and so on. Nevertheless, the controller can not reach high enough resolution/speed for specific tasks, and its control gains need to be tuned repeatedly for different probes or distinct samples, which has always been a great challenge for inexperienced operators. To achieve better performance, in the literature, some advanced control methods, such as robust repetitive control [8], iterative learning control [9], and so on, have been proposed to increase system bandwidth and improve robustness over various disturbance and measurement noise. Unfortunately, most of the aforementioned methods are only applicable for static mode AFMs.

With the increasing requirements of little or no harm to samples, more and more focus has been put on the research of dynamic AFMs. Recently, some investigation has been implemented to explore the complex dynamics of the cantilevers, and the obtained results can be roughly classfied as analytical descriptions of AM-AFM [10], harmonic balance method [11], and so on. However, these results are usually too complex to be utilized for AM-AFM controller design and analysis. Due to this reason, some researchers make efforts to improve the imaging speed of AFMs directly through signal processing techniques. For example, based on the construction of an observer, some transient signal is employed in [12] for fast imaging. More recently, Fang *et al.* propose a variable-speed scanning (VSS) method in [13] for an AFM, which tunes the scanning speed online based on the feedback information to properly distribute imaging time along sample surface. As shown by experimental results, this VSS method speeds up the imaging rate successfully. Yet, these methods are mainly empirical, whose performance heavily depends on the nature of the measured samples.

So far, when utilizing an AFM instrument, an operator has to spend much time in seeking out the best parameters to obtain satisfactory imaging performance. To alleviate this burden, some adaptive strategies have been successfully introduced into AFMs to automate the parameter-adjusting task. For instance, an adaptive control approach is propose in [14] to eliminate the need of manually tuning control gains for different scanning tasks, and in [15], Fang *et al.* design an intelligent PI controller with relay-based tuning mechanism for contact-mode AFMs, which successfully automates the tuning procedure for the control gains. Apparently, these methods largely decrease operation difficulty, especially for those inexperienced manipulators. Unfortunately, they are only available for contact-mode AFMs. Moreover, the output saturation phenomenon, which happens frequently in AFMs due to

This work was supported by the Special Fund for Basic Research on Scientific Instruments of the Chinese National Natural Science Foundation (61127006).

All the authors are with the Institute of Robotics and Automatic Information System, Nankai University, Tianjin 300071, China (email: y-fang@robot.nankai.edu.cn).

measurement constraint, is usually neglected when analyzing the performance of an AFM system. Yet, it is a generally accepted fact that saturation degrades the performance of a control system badly, and it thus needs to be considered carefully [16], [17].

To overcome the drawbacks in current AM-AFM systems, in this research, we study the behavior of an AM-AFM system and propose an output feedback robust adaptive control (OFRAC) strategy to enable an AM-AFM system to complete high-speed scanning tasks. More specifically, since it is difficult to deduce the theoretical expression of the cantilever oscillation amplitude in terms of tip-sample separation by solving the complicated nonlinear equation, a control-oriented reduced model is firstly presented for this mapping on the basis of both theoretical analysis and experimental study. Subsequently, an OFRAC strategy is proposed for an AM-AFM system with the saturation problem fully considered, whose performance is guaranteed by rigorous analysis. The proposed method is then employed in a virtual AM-AFM system, with the results clearly demonstrating the advantages of the designed OFRAC strategy over current methods. The contribution of the paper lies in the fact that it obtains a practical control-oriented model with satisfactory accuracy, based on which some output feedback control is proposed to successfully solve sensor saturation and various disturbance rejection problems for AM-AFMs, and thus to improve the performance of high-speed AFMs remarkably.

The rest of this paper is organized as follows. In Section II, the basic working principle of dynamic-mode AFMs is briefly introduced. The overall system model is presented in Section III. In Section IV, an OFRAC strategy is designed in detail, which is utilized and sufficiently tested in a virual AFM system in Section V. Finally, Section VI summarizes this research and presents some plans for the future work.

II. Dynamic Atomic Force Microscopy

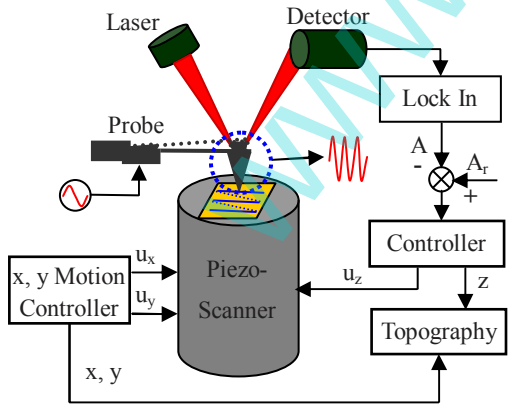

Fig. 1. Schematic diagram of a dynamic AFM.

As shown in Fig. 1, a typical dynamic AFM is composed of four parts: microcantilever/probe, laser detector, piezo-scanner and digital controller. According to the types of feedback signals, two major operating dynamic AFM modes have been developed: amplitude modulation (AM)-AFM and frequency modulation (FM)-AFM in which the oscillation amplitude and resonant frequency is utilized as the regulated signal respectively.

In the AM-AFM mode, the cantilever is excited by a sinusoidal actuating signal around its resonant frequency. When the probe is brought close enough to the sample (within several nanometers), its oscillating amplitude will be influenced by the complex interaction force between the sample and the probe tip. The varying amplitude can be measured by a laser detector and a lock-in circuit, which is then employed as the feedback signal. For this sample-scanning type AFM (see Fig. 1), the tip-sample separation is regulated by the piezo-scanner displacement in the z-axis to keep the oscillation amplitude of the cantilever at a given constant. At the same time, the sample is moved in a raster scan mode with the piezo-scanner in the x-y plane. Then, the x-y coordinates, together with the corresponding displacement of the piezo-scanner in the z-axis, are recorded to characterize the sample topography.

III. Model Analysis and Experimental Verification

In this section, we will discuss the overall behavior of AM-AFMs, including the piezo-scanner dynamics in the z-axis, the relationship between tip-sample separation and cantilever oscillation amplitude, and some other amplifier gains.

A. Piezo-Scanner Dynamics

A piezoelectric actuator is the most widely utilized micro/nano positioner due to its advantages of high resolution, fast frequency response, and so on [18], [19]. However, the structural vibration dynamics as well as the hysteresis nonlinearity are the main factors that limit its further applications [20], [21], [22]. In the z-axis of a typical piezo-tube scanner utilized in an AFM system, since the displacement is comparatively small, the hysteresis behavior is not remarkable. Hence, in this research, only the structural dynamics is considered when designing the control law. Compared with the conventional second-order spring-mass-damper model [23], the higher-order model in [24] is capable of capturing the high frequency part of the piezo-scanner dynamics which can not be neglected in dynamic AFM systems. Therefore, the following transfer function is adopted to describe the piezo-scanner dynamics [24]:

$$\begin{aligned} Y(s) &= k_s \frac{b_{n-1}s^{n-1} + b_{n-2}s^{n-2} + \cdots + b_1 s + b_0}{s^n + a_{n-1}s^{n-1} + \cdots + a_1 s + a_0} U(s) \\ &= k_s G(s) U(s) \end{aligned} \tag{1}$$

where $Y(s)$ and $U(s)$ are the Laplace transforms of the output displacement $y(t) \in \mathbb{R}$ and input voltage $u(t) \in \mathbb{R}$ respectively, $[a_0, \cdots, a_{n-1}]^{\mathrm{T}} \in \mathbb{R}^n$, $[b_0, \cdots, b_{n-1}]^{\mathrm{T}} \in \mathbb{R}^n$ are the system parameters, and $k_s \in \mathbb{R}^+$ denotes the deformation coefficient. Because only the output is measurable in a dynamic AFM system, an observer is needed to estimate the state of the system. Based on this reason, (1) is rewritten into

the following state-space form:

$$\begin{aligned} \dot{x}_1 &= -a_{n-1}x_1 + x_2 + b_{n-1}u \\ \dot{x}_2 &= -a_{n-2}x_1 + x_3 + b_{n-2}u \\ &\vdots \\ \dot{x}_{n-1} &= -a_1 x_1 + x_n + b_1 u \\ \dot{x}_n &= -a_0 x_1 + b_0 u \\ y &= k_s x_1 \end{aligned} \tag{2}$$

which can be further re-written into a more compact form as

$$\begin{aligned} \dot{x} &= Ax + Bu \\ y &= k_s Cx \end{aligned} \tag{3}$$

with the vector $x \in \mathbb{R}^n$ and the matrices $A \in \mathbb{R}^{n\times n}, B \in \mathbb{R}^n, C \in \mathbb{R}^{1\times n}$ explicitly defined as:

$$\begin{aligned} x &= \begin{bmatrix} x_1 & x_2 & \cdots & x_n \end{bmatrix}^{\mathrm{T}} \\ A &= \begin{bmatrix} -a_{n-1} & & & \\ -a_{n-2} & & I_{n-1} & \\ \vdots & & & \\ -a_0 & 0 & \cdots & 0 \end{bmatrix}, B = \begin{bmatrix} b_{n-1} \\ b_{n-2} \\ \vdots \\ b_0 \end{bmatrix} \\ C &= \begin{bmatrix} 1 & 0 & \cdots & 0 \end{bmatrix}. \end{aligned} \tag{4}$$

It is straightforward to show that the system in this form is observable. Based on the property of AFM systems, it is assumed that the plant order n is known, and the relative degree is 1. Besides, the high frequency gain is assumed to be positive in the sense that $b_{n-1} > 0$.

B. Relationship between Tip-Sample Separation and Oscillation Amplitude

When scanning a sample with an AFM, the tip-sample separation varies with the sample topography and the piezo-scanner displacement. The variation of the separation distance affects the oscillation amplitude of the cantilever. Due to the complex tip-sample interaction, it is difficult to obtain the exact function from the tip-sample separation to the cantilever oscillation amplitude which will be discussed in this subsection.

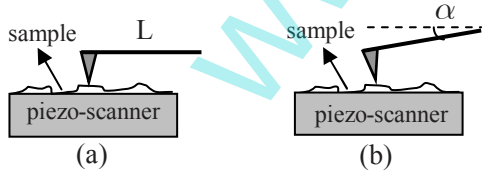

Fig. 2. Installation angle of the cantilever: (a) parallel with the sample platform; (b) with an angle α between them.

Ideally, the probe is equipped parallel with the sample platform as shown in Fig. 2 (a). However, in actual AFM systems, there usually exists an angle offset between them (Fig. 2 (b)). Thus, the separation $s(t) \in \mathbb{R}$ between the sample and the initial position of the probe can be expressed as

$$s(t) = \frac{s_0 - (y(t) + d_0(t))}{cos\alpha} \tag{5}$$

where $s_0 \in \mathbb{R}$ denotes the initial distance, $d_0(t) \in \mathbb{R}$ is the sample topography which is considered as time-varying disturbance entering into the system, $y(t) \in \mathbb{R}$ represents the displacement of the piezo-scanner, and $\alpha \in \mathbb{R}^+$ represents the angle offset between the cantilever and the sample platform.

Generally, the cantilever dynamics is described by the following Luré equation [25]:

$$\ddot{p}_c + \frac{\omega_0}{Q}\dot{p}_c + \omega_0^2 p_c = \left(F_0 \cos\omega t + F_{ts}(s + p_c)\right)/m \tag{6}$$

where $p_c(t)$, $\dot{p}_c(t)$, $\ddot{p}_c(t) \in \mathbb{R}$ are the position, velocity and acceleration of the cantilever movement. $F_0 \cos\omega t$ denotes the actuating signal, m, ω_0 and Q are the effective mass, natural frequency and quality factor of the cantilever respectively, and the nonlinear tip-sample interaction function $F_{ts}(s + p_c)$ can be expressed by the Maugis model [26].

In the AM-AFM system, the controlled signal is the oscillation amplitude. Thus, it is required to calculate the oscillation amplitude of the cantilever $z_c(t) \in \mathbb{R}$ in terms of the tip-sample separation $s(t)$, which is the stable solution of (6). Unfortunately, it is difficult to solve the nonlinear differential equation (6). Several analytical or semi-analytical approaches, such as virial theorem [27], harmonic balance method [11], and so on, have been proposed to describe the behavior of the amplitude and phase offset. However, these methods usually yield solutions involved with extremely complicated expressions which are difficult to be employed for controller design.

Considering the fact that the tip interacts with the sample only when it vibrates towards the end of the negative cycle, and summarizing many simulation/experimental results, it is common practice that the cantilever will oscillate with the free oscillation amplitude $z_0 \in \mathbb{R}^+$ when the tip-sample separation $s(t)$ is greater than z_0, and stop oscillating when $s(t)$ approaches 0. Thus, the following saturation function is proposed for controller design without losing much accuracy:

$$z_c(t) = \mathrm{sat}_{0,z_0}(s(t)) + d_1(t) \tag{7}$$

where the saturation function is defined as

$$\mathrm{sat}_{0,z_0}(s) = \begin{cases} z_0 & s \geq z_0 \\ s & 0 < s \leq z_0 \\ 0 & s \leq 0 \end{cases} \tag{8}$$

and $d_1(t) \in \mathbb{R}$ denotes the unmodeled bounded disturbance. To further interpret this model, an experiment is implemented on a Benyuan CSPM 4000 system, with the results provided in Fig. 3 to describe the relationship between tip-sample separation and cantilever oscillation amplitude. In Fig. 3, the solid and dashed lines represent the approaching and departing processes respectively. It can be seen that when the tip-sample separation exceeds its free oscillation value, the amplitude becomes a constant. Besides, the amplitude of the cantilever is nearly zero when the tip contacts with the sample. Therefore, the reduced model (8) is able to describe the nonlinear separation-amplitude relationship with much accuracy.

As stated previously, when saturation happens, either the tip-sample interaction has no effect (free oscillation) or the cantilever stops oscillating, thus the detected signal can not

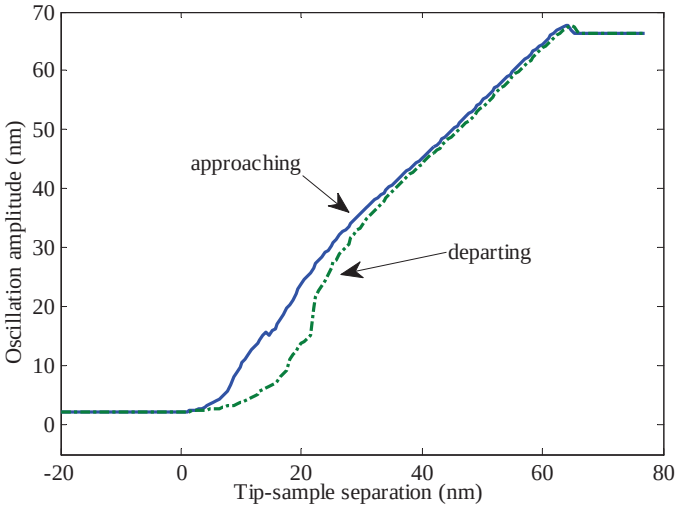

Fig. 3. Experimental results: oscillation amplitude vs. tip-sample separation.

exactly reflect the system error. For brevity, the case of free oscillation is subsequently taken as an example to discuss the performance of the presented control technique. Nevertheless, the analysis is also valid for the case of stopping oscillation. In this case, (7) turns into the following relationship:

$$z_c(t) = \text{sat}_{z_0}(s(t)) + d_1(t) \tag{9}$$

Furthermore, in the AM-AFM system, the deflection angle, rather than the movement of the cantilever, is obtained by a laser detector to facilitate subsequent feedback control. Then, a lock-in amplifier converts this signal into the final oscillation amplitude $z_p(t) \in \mathbb{R}$ in the following form:

$$z_p = k_p \frac{z_c}{L} \tag{10}$$

where $k_p \in \mathbb{R}^+$ is the detector gain, while $L \in \mathbb{R}^+$ represents the cantilever length.

Based on the previous analysis, combining (3), (5), (9) and (10) yields the overall model of the AM-AFM system:

$$\begin{aligned} \dot{x} &= Ax + Bu \\ z_p &= \text{sat}_{z_1}\big(k_1(s_0/k_s - (Cx + d_0/k_s))\big) + d_2 \end{aligned} \tag{11}$$

where $z_1 \in \mathbb{R}^+$ denotes the upper bound of the saturation function, $d_2(t) \in \mathbb{R}$ is a bounded term containing both unmodeled disturbance and measurement noise, $k_1 \in \mathbb{R}^+$ is an unknown positive parameter which is described by

$$k_1 = k_s k_p / (L cos\alpha), \tag{12}$$

and A, B, C, k_p, k_s, L, and α have been defined previously, which vary with different scanning tasks. Therefore, these signals are assumed unknown during the subsequent controller design. In addition, $d_0(t)$ represents the sample surface topography defined in (5), which is always bounded.

Remark 1: For the system (11), though the top equation is linear, the bottom equation for the output is very complex as the measurement is contaminated by sensor saturation and various disturbances, which then makes it very difficult to regulate the output z_p around some setpoint, especially when only the saturated output is available for feedback. Therefore, the subsequent part aims to propose an ambitious nonlinear control law to address the sensor saturation and disturbance rejection problems simultaneously in the context of output feedback.

Remark 2: It should be noted that the active Q control strategy [28], which can fasten the probe/cantilever response remarkably, has been widely utilized in AM-AFM systems. Therefore, it is reasonable in this research to describe the behavior of the cantilever by a static function, because owing to the employment of the active Q control algorithm, the oscillation amplitude follows well with the variation of the tip-sample separation.

IV. Controller Design

In AFM systems, the oscillation amplitude of the cantilever cannot be observed from the tip-sample separation when it is beyond a known threshold (such as the step up or down of the sample). In this section, a robust adaptive controller is designed to regulate the cantilever oscillation amplitude around the setpoint $z_r < z_1 \in \mathbb{R}$. To this end, the control error $e(t) \in \mathbb{R}$ is defined as follows:

$$e = z_r - z_p. \tag{13}$$

Obviously, due to the saturation problem, it is very difficult to analyze the behavior of the output $z_p(t)$. Based on this fact, the following auxiliary output signal $z_p'(t) \in \mathbb{R}$ is defined:

$$z_p' = k_1(s_0/k_s - (Cx + d_0/k_s)) + d_2, \tag{14}$$

and the auxiliary error signal $e'(t) \in \mathbb{R}$ is correspondingly defined as:

$$e' = z_r - z_p'. \tag{15}$$

Based on the previous definitions, the control error $e(t)$ is related to the auxiliary signal $e'(t)$ in the following manner:

$$e = \text{sat}_{e_0}(e') \tag{16}$$

where the saturation function is defined as

$$\text{sat}_{e_0}(e') = \begin{cases} e_0 & e' \le e_0 \\ e' & e' > e_0 \end{cases} \tag{17}$$

and

$$e_0 = z_r - z_1 - d_2 < 0. \tag{18}$$

Based on the relationship of (16) and (17), $e(t)$ can be reformulated as

$$e = \gamma(e')e' \tag{19}$$

where

$$\gamma(e') = \begin{cases} \dfrac{e_0}{e'} & e' \le e_0 \\ 1 & e' > e_0. \end{cases} \tag{20}$$

Therefore, based on (13), (15) and (19), the relationship of z_p and z_p' can be calculated as:

$$z_p = z_p' + (1 - \gamma)e'.$$

Because only the output $z_p(t)$ is measurable in AM-AFM systems, an observer is first constructed to estimate the system state for the subsequent output feedback controller.

A. K-filter Construction

Based on the characteristics of the AFM systems, we need to address the output feedback control problem with uncertainties [29]. Therefore, an observer is needed to estimate the unmeasurable system state [30]. To this end, the first equation of (11) is rewritten as:

$$\dot{x} = \bar{A}x + \frac{a^* - k}{k_1} z_p + (k - a^*)\left(\frac{s_0 - d_0}{k_s} + \frac{d_2}{k_1}\right) + Bu \quad (21)$$

where $a^* = [a_{n-1}, a_{n-2}, \cdots, a_0]^T$, and the matrix

$$\bar{A} = A^* - k\zeta_1^T \quad (22)$$

with

$$A^* = \begin{bmatrix} 0 & & \\ \vdots & I_{n-1} & \\ 0 & \cdots & 0 \end{bmatrix},$$

ζ_1 denoting the unit vector with the first element being 1. In (21), the observer gain vector $k \in \mathbb{R}^n$ is selected suitably to make the matrix $\bar{A}$ Hurwitz. That is, there exists a positive symmetric matrix P satisfying:

$$\bar{A}^T P + P\bar{A} = -I, \quad P = P^T, \quad P > 0. \quad (23)$$

Based on the system property, we define new states $\xi_n, \xi_i, v_i \in \mathbb{R}^n, 0 \le i \le n-1$:

$$\begin{aligned} \dot{\xi}_n &= \bar{A}\xi_n + kz_p \\ \dot{\xi}_i &= \bar{A}\xi_i + \zeta_{n-i} z_p \quad 0 \le i \le n-1 \\ \dot{v}_i &= \bar{A}v_i + \zeta_{n-i} u \quad 0 \le i \le n-1, \end{aligned} \quad (24)$$

then the state can be estimated as:

$$\hat{x} = -\frac{1}{k_1}\xi_n + \frac{1}{k_1}\sum_{i=0}^{n-1}(\xi_i a_i) + \sum_{i=0}^{n-1}(v_i b_i) \quad (25)$$

$$\begin{aligned} \dot{\hat{x}} &= \bar{A}\hat{x} + \frac{a^* - k}{k_1} z_p + Bu \\ &= \bar{A}\hat{x} + \frac{a^* - k}{k_1} z_p' + \frac{a^* - k}{k_1}(1-\gamma)e' + Bu. \end{aligned} \quad (26)$$

Furthermore, define estimation error $\varepsilon_x = x - \hat{x}$, then

$$\dot{\varepsilon}_x = \bar{A}\varepsilon_x + (k - a^*)\left(\frac{s_0 - d_0}{k_s} + \frac{d_2}{k_1}\right) - \frac{a^* - k}{k_1}(1-\gamma)e'. \quad (27)$$

To facilitate the following analysis, we separate ε_x into two parts of ε and ε_u, with

$$\dot{\varepsilon} = \bar{A}\varepsilon - \frac{a^* - k}{k_1}(1-\gamma)e' \quad (28)$$

and

$$\dot{\varepsilon_u} = \bar{A}\varepsilon_u + (k - a^*)\left(\frac{s_0 - d_0}{k_s} + \frac{d_2}{k_1}\right). \quad (29)$$

As the latter term in the right-hand side of (29) can be bounded by a known positive constant T:

$$|(k - a^*)\left(\frac{s_0 - d_0}{k_s} + \frac{d_2}{k_1}\right)| < T,$$

then

$$\varepsilon_u \in \Omega_\varepsilon \triangleq \{\varepsilon_u : |\varepsilon_u| \le \delta_\varepsilon\} \quad (30)$$

where δ_ε is defined as

$$\delta_\varepsilon = T\int_0^t e^{\bar{A}(t-\tau)} d\tau.$$

B. Robust Adaptive Controller Design

Based on the constructed filter, a robust adaptive controller is designed to achieve desired performance. From (11), (14) and (15), the auxiliary error dynamics can be calculated as:

$$\dot{e}' = k_1\dot{x}_1 + k_1\dot{d}_0/k_s - \dot{d}_2. \quad (31)$$

In addition, it can be deduced from (25) that

$$\begin{aligned} \dot{x}_1 &= x_2 + \frac{a_{n-1}}{k_1} z_p - a_{n-1}\left(\frac{s_0 - d_0}{k_s} + \frac{d_2}{k_1}\right) + b_{n-1}u \\ x_2 &= -\frac{1}{k_1}\xi_{n,2} + \frac{1}{k_1}\xi_{(2)}a^* + v_{(2)}B + \varepsilon_{x_2} \end{aligned} \quad (32)$$

where

$$\begin{aligned} \xi_{(2)} &= [\xi_{n-1,2}, \cdots, \xi_{0,2}] \\ v_{(2)} &= [v_{n-1,2}, \cdots, v_{0,2}] \\ \varepsilon_{x_2} &= \zeta_2^T \varepsilon_x = \varepsilon_2 + \varepsilon_{u_2}. \end{aligned} \quad (33)$$

After some mathematical manipulations, the auxiliary error dynamics (31) can be rewritten as

$$\begin{aligned} \dot{e}' = &-\xi_{n,2} + (\omega^T - (1-\gamma)e'\zeta_1^T)\theta + v_{n-1,2}k_1 b_{n-1} \\ &+ \Delta + k_1\varepsilon_2 + b_{n-1}k_1 u \end{aligned} \quad (34)$$

where the signals $v_{(2)}^*$, B^{*T} are selected as the last $n-1$ columns of $v_{(2)}$ and B^T:

$$\begin{aligned} v_{(2)}^* &= [v_{n-2,2}, \cdots, v_{0,2}] \\ B^* &= [b_{n-2}, \cdots, b_0]^T, \end{aligned} \quad (35)$$

and the signals ω, θ, and Δ are explicitly defined as follows:

$$\begin{aligned} \omega &= [z_p\zeta_1^T + \xi_{(2)}, v_{(2)}^*]^T \\ \theta &= [a^{*T}, k_1 B^{*T}]^T \\ \Delta &= -a_{n-1}k_1 s_0/k_s + a_{n-1}k_1 d_0/k_s \\ &\quad -a_{n-1}d_2 + k_1\dot{d}_0/k_s - \dot{d}_2 + k_1\varepsilon_{u_2}. \end{aligned} \quad (36)$$

From the previous analysis, we know that b_{n-1} and k_1 are both positive, then (34) can be reformulated as:

$$\begin{aligned} \frac{\dot{e}'}{b_{n-1}k_1} = &-\frac{\xi_{n,2}}{b_{n-1}k_1} + \frac{\omega^T\theta}{b_{n-1}k_1} - \frac{(1-\gamma)e'\zeta_1^T\theta}{b_{n-1}k_1} \\ &+ \frac{\Delta}{b_{n-1}k_1} + v_{n-1,2} + \frac{\varepsilon_2}{b_{n-1}} + u. \end{aligned} \quad (37)$$

Assuming that the disturbance and the sample topography are both bounded, it can be shown that Δ is bounded as:

$$|\Delta| \le M$$

where M is a positive constant. To transform (37) into a more compact form to facilitate controller design, we define the following signals:

$$\begin{aligned} W &= [-\xi_{n,2} + \mathrm{sgn}(e)M, \omega^T]^T \\ W_1 &= [-\xi_{n,2}, \omega^T]^T \\ \Phi &= \left[\frac{1}{b_{n-1}k_1}, \frac{\theta^T}{b_{n-1}k_1}\right]^T \end{aligned} \quad (38)$$

where Φ is the unknown parameters vector. For a practical AFM system, Φ is always bounded in the sense that:

$$\Phi \in \Omega_\Phi \triangleq \{\Phi : \Phi_{\min} \leq \Phi \leq \Phi_{\max}\} \tag{39}$$

where $\Phi_{\min}$ and $\Phi_{\max}$ are the infimum and supremum of Φ respectively. After some mathematical manipulations, the error system (37) can be expressed as:

$$\begin{aligned}\frac{\dot{e'}}{b_{n-1}k_1} = W^T\Phi + \frac{\Delta - \text{sgn}(e)M}{b_{n-1}k_1} + v_{n-1,2} \\ + \frac{\varepsilon_2}{b_{n-1}} - \frac{(1-\gamma)e'\zeta_1^T\theta}{b_{n-1}k_1} + u\end{aligned} \tag{40}$$

where the fact of $\text{sgn}(e') = \text{sgn}(e)$ from (18), (19) and (20) has been utlized. For system (40) with unknown parameter vector Φ and bounded disturbance Δ, the following robust adaptive control law is designed to deal with these model uncertainties:

$$u = u_1 + u_2 \tag{41}$$

where the component

$$u_1 = -W_1^T\hat{\Phi} - v_{n-1,2} - k_e e \tag{42}$$

is introduced to deal with parameters uncertainty, with k_e denoting a positive, constant control gain, $\hat{\Phi}$ representing the estimation of the unknown parameters vector Φ. To cease parameter adaptation in this algorithm, the μ-modification scheme is employed to design the update law [31] :

$$\dot{\hat{\Phi}} = \text{Proj}_{\hat{\Phi}}\left(\Gamma(eW - \mu\hat{\Phi})\right) \tag{43}$$

where Γ is a positive definite diagonal matrix, the projection function is defined as

$$\text{Proj}_{\hat{\Phi}}(\cdot) = \begin{cases} 0 & \text{for} \quad \hat{\Phi} = \Phi_{\max} \quad \text{and} \quad \cdot > 0 \\ 0 & \text{for} \quad \hat{\Phi} = \Phi_{\min} \quad \text{and} \quad \cdot < 0 \\ \cdot & \text{else} \end{cases} \tag{44}$$

and μ is defined in the following form:

$$\mu = \begin{cases} k_\mu(c_1 - |e|) & \text{for} \quad |e| < c_1 \\ 0 & \text{else} \end{cases} \tag{45}$$

where k_μ is a positive constant, $c_1 < |e_0|$ specifies the desired error bound which is also a positive constant. From (44), it is straightforward to conclude the following two facts:

$$\begin{aligned}&\hat{\Phi} \in \Omega_\Phi = \left\{\hat{\Phi} : \Phi_{\min} \leq \hat{\Phi} \leq \Phi_{\max}\right\} \\ &\tilde{\Phi}\Gamma^{-1}\text{Proj}_{\hat{\Phi}}(\cdot) \geq \tilde{\Phi}\Gamma^{-1}\cdot \quad \forall\cdot\end{aligned} \tag{46}$$

which will be utilized for the stability analysis. Subsequently, the robust part of the controller is designed as:

$$u_2 = -\frac{M^2 e}{M|e| + c_2}\zeta_1^T\hat{\Phi} \tag{47}$$

where c_2 is a sufficiently small positive constant. After substituting the control law (41), (42), (43) and (47) into system (40), we can obtain the closed-loop error system:

$$\begin{aligned}\frac{\dot{e'}}{b_{n-1}k_1} = W_1^T\tilde{\Phi} - (1-\gamma)e'\zeta_1^T\frac{a^*}{b_{n-1}k_1} + \Delta\zeta_1^T\Phi \\ - \frac{M^2\gamma e'}{M|\gamma e'| + c_2}\zeta_1^T\hat{\Phi} + \frac{\varepsilon_2}{b_{n-1}} - k_e\gamma e'\end{aligned} \tag{48}$$

where the estimation error $\tilde{\Phi}$ is defined as:

$$\begin{aligned}\tilde{\Phi} &= \Phi - \hat{\Phi} \\ \dot{\tilde{\Phi}} &= -\dot{\hat{\Phi}}.\end{aligned} \tag{49}$$

Remark 3: The introduction of the auxiliary signals $z'_p(t)$ in (14) and $e'(t)$ in (15) aims to provide some convenience for the analysis of the system dynamics and to facilitate the control design. However, since these signals are unavailable due to the saturation problem, they are not utilized to construct the control law. That is, the analysis for the dynamics of the auxiliary signal $e'(t)$ aims to provide some hints for the controller design since it is very difficult to analyze the dynamics of $e(t)$ due to the presence of the saturation component. However, the control law is only based on the real error signal $e(t)$.

C. Stability Analysis

In this section, the performance of the proposed control algorithm is illustrated by two theorems which will be proven afterward. Specifically, the analysis is implemented in two steps. In the first step, it is shown that the presented controller will push the system away from the saturation area in some finite time, which is supported by Theorem 1. In the second step, it is proven that when there is no saturation, the control law drives the control error into the pre-defined error bound, as explicitly stated in Theorem 2.

Theorem 1. For the saturation case of the system described by (11), the control input (42) and (47), together with the update law (43), ensures that the error system (40) enters the set $E_1 \triangleq \{e' : |e'| < |e_0|\}$ in some finite time from a certain saturation region which can be calculated rigorously.

Proof: When saturation occurs, the following facts of

$$e' \leq e_0 = e = \gamma e' < 0 \tag{50}$$

and

$$\mu = 0 \tag{51}$$

can be obtained from (17), (18), (19), (20) and (45), which will be utilized for the subsequent analysis.

To verify the effectiveness of the above control laws in the case of saturation, we define the following Lyapunov function candidate:

$$V_1 = \frac{e_0}{b_{n-1}k_1}e' + \frac{1}{2}\tilde{\Phi}^T\Gamma^{-1}\tilde{\Phi} + \frac{2}{k_e b_{n-1}^2}\varepsilon^T P\varepsilon. \tag{52}$$

By utilizing the fact of (50), we can take the time derivative of (52) to obtain

$$\dot{V}_1 = \frac{\gamma e'\dot{e'}}{b_{n-1}k_1} - \tilde{\Phi}^T\Gamma^{-1}\dot{\hat{\Phi}} + \frac{2}{k_e b_{n-1}^2}(\dot{\varepsilon}^T P\varepsilon + \varepsilon^T P\dot{\varepsilon}). \tag{53}$$

Then, substituting (28), (43) and (48) into (53) yields:

$$\begin{aligned}\dot{V}_1 \leq &\left(-k_e\gamma^2 - (1-\gamma)\gamma\zeta_1^T\frac{a^*}{b_{n-1}k_1} + \frac{1}{4}k_e\gamma^2\right)e'^2 \\ &+\frac{4(1-\gamma)^2}{k_e b_{n-1}^2}\left(\frac{a^*-k}{k_1}\right)^T PP\left(\frac{a^*-k}{k_1}\right)e'^2 \\ &+\zeta_1^T\hat{\Phi}c_2.\end{aligned} \tag{54}$$

where the fact of (51) has been utilized. From (54), we can solve the inequality

$$g(\gamma) \triangleq -\chi_1\gamma^2-\chi_2(1-\gamma)\gamma+\chi_3(1-\gamma)^2 \leq -\frac{\zeta_1^T\Phi_{\max}c_2+c_3}{c_1^2} \tag{55}$$

to obtain the attractive region, where c_1 and c_2 have been defined previously while c_3 is an arbitrary positive constant, and the signals

$$\chi_1 = \frac{3}{4}k_e \tag{56}$$

$$\chi_2 = \frac{\zeta_1^T a^*}{b_{n-1}k_1} \tag{57}$$

$$\chi_3 = \frac{4}{k_e b_{n-1}^2}\left(\frac{a^*-k}{k_1}\right)^T PP\left(\frac{a^*-k}{k_1}\right) \tag{58}$$

are all positive. If the solution of (55) contains all values in $(0,1)$, the global uniform ultimate boundedness(GUUB) result can be obtained. Otherwise, by calculating (55), the infimum of γ is defined as:

$$\gamma^* \triangleq \inf\{\gamma \in (0,1] : g(\gamma) \leq -\frac{\zeta_1^T\Phi_{\max}c_2+c_3}{c_1^2}\}. \tag{59}$$

Then, define

$$\Omega_{V_1} \triangleq \left\{e', \tilde{\Phi}, \varepsilon \mid V_1(e', \tilde{\Phi}, \varepsilon) \leq \frac{1}{b_{n-1}k_1}\frac{e_0^2}{\gamma^*}\right\}, \tag{60}$$

it can be seen that Ω_{V_1} is a positive invariant set. That is, for any $e(0) \in \Omega_{V_1}$, we know that $e'(t) \in \Omega_{V_1}$ when $t > 0$. And as $|e_0| > c_1$, $|e'(t)|$ will be less than $|e_0|$ in some finite time when saturation happens. Additionally, define a set for the auxiliary tracking error $e'(t)$ and observer error ε:

$$\begin{aligned}\Omega_{e',\varepsilon} \triangleq \Big\{ & e', \varepsilon \mid \frac{e_0}{b_{n-1}k_1}e' + \frac{2}{k_e b_{n-1}^2}\varepsilon^T P\varepsilon \\ & \leq \frac{1}{b_{n-1}k_1}\frac{e_0^2}{\gamma^*} - \frac{1}{2}\tilde{\Phi}_{\max}^T\Gamma^{-1}\tilde{\Phi}_{\max}\Big\},\end{aligned} \tag{61}$$

then for any $(e',\ \varepsilon)$ starting from $\Omega_{e',\varepsilon}$, in a finite time, $e'(t)$ will go into the set $\Omega_{e'} \triangleq \{e'(t)\ : |e'(t)| \leq |e_0|\}$. ■

Based on the previous analysis, for the calculated attractive region, the saturation will disappear and the controlled error can be measured eventually. Afterward, $e' > e_0$ and $\gamma = 1$, which implies the fact of $e' = e$.

Theorem 2. When the saturation disappears, for the system governed by (11), the control input (41), (42) and (47), together with the update law (43), ensures that the error system (40) enters the set $E_0 \triangleq \{e :\ |e| < c_1\}$ in some finite time, with c_1 standing for the pre-defined allowable error bound defined in (45).

Proof: To prove Theorem 2, we define the following nonnegative Lyapunov function candidate:

$$V_2 = \frac{1}{2}\frac{1}{b_{n-1}k_1}e^2 + \frac{1}{2}\tilde{\Phi}^T\Gamma^{-1}\tilde{\Phi} + \left(k_2 + \frac{1}{k_e b_{n-1}^2}\right)\varepsilon^T P\varepsilon \tag{62}$$

where k_2 is a positive constant. After taking the time derivative of (62), we obtain:

$$\dot{V}_2 = \frac{e\dot{e}}{b_{n-1}k_1} - \tilde{\Phi}^T\Gamma^{-1}\dot{\hat{\Phi}} - \left(k_2 + \frac{1}{k_e b_{n-1}^2}\right)\varepsilon^T\varepsilon. \tag{63}$$

Substituting (48) and (43) into (63), and utilizing (46) on the resulting expression yields:

$$\begin{aligned}\dot{V}_2 \leq & \left(-k_e + \frac{k_e}{4}\right)e^2 - \mu\tilde{\Phi}^T\tilde{\Phi} + \mu\tilde{\Phi}^T\Phi \\ & - k_2\varepsilon^T\varepsilon + \zeta_1^T\hat{\Phi}c_2.\end{aligned} \tag{64}$$

Subsequently, the facts of $0 < \zeta_1^T\hat{\Phi} \leq \zeta_1^T\Phi_{\max}$ and

$$\tilde{\Phi}^T\hat{\Phi} \leq -\frac{1}{2}\tilde{\Phi}^T\tilde{\Phi} + \frac{1}{2}\Phi^T\Phi \tag{65}$$

are further employed to obtain the following result:

$$\begin{aligned}\dot{V}_2 \leq & -\frac{3}{4}k_e e^2 - \frac{1}{2}\mu\tilde{\Phi}^T\tilde{\Phi} - k_2\varepsilon^T\varepsilon \\ & + \frac{1}{2}\mu\Phi^T\Phi + \zeta_1^T\Phi_{\max}c_2.\end{aligned} \tag{66}$$

Particularly, when $|e| \geq c_1$, we have

$$\dot{V}_2 \leq -\frac{3}{4}k_e e^2 + \zeta_1^T\Phi_{\max}c_2. \tag{67}$$

Therefore, by choosing k_e such that

$$k_e \geq \frac{4}{3}\frac{\zeta_1^T\Phi_{\max}c_2+c_3}{c_1^2} \tag{68}$$

with c_1, c_2, c_3 being defined previously, $\dot{V}_2$ can be further upper-bounded as:

$$\dot{V}_2 \leq -c_3, \quad \forall\ |e| \geq c_1. \tag{69}$$

Since $\dot{V}_2$ is continuous with respect to $e(t)$, there exists a constant $0 < c_1' < c_1$ such that

$$\forall\ |e(t)| \geq c_1', \quad \dot{V}_2 < 0. \tag{70}$$

Note that $c_1' < c_1$ implies that the system error $|e(t)|$ will be less than c_1 in some finite time. From (45), it is straightforward to conclude that when $|e(t)| < c_1'$,

$$k_\mu(c_1 - c_1') \leq \mu \leq k_\mu c_1. \tag{71}$$

Then, based on the definition of $\delta_{c_1} = c_1 - c_1' > 0$, (66) can be rearranged as

$$\dot{V}_2 \leq -k'V_2 + \frac{1}{2}k_\mu c_1\Phi^T\Phi + \zeta_1^T\Phi_{\max}c_2 \tag{72}$$

where

$$\begin{aligned}k' = \min\Bigg(& \frac{\frac{3}{4}k_e}{\frac{1}{2b_{n-1}k_1}}, \frac{\frac{1}{2}k_\mu\delta_{c_1}}{\frac{1}{2}\lambda_{\max}(\Gamma^{-1})}, \\ & \frac{k_2}{\left(k_2 + \frac{1}{2k_e b_{n-1}^2}\right)\lambda_{\max}(P)}\Bigg)\end{aligned} \tag{73}$$

with $\lambda_{\max}(*)$ denoting the maximum eigenvalue of $*$.
By solving (72), we can obtain

$$V_2(t) \leq \frac{\frac{1}{2}k_\mu c_1\Phi^T\Phi + \zeta_1^T\Phi_{\max}c_2}{k'}\left(1 - e^{-k't}\right) + V_2(0)e^{-k't}. \tag{74}$$

Therefore, $V_2(t) \in \mathcal{L}_\infty$. Consequently, from (62), we know that $e(t)$, $\hat{\Phi}(t)$ and $\varepsilon(t)$ are all bounded. Furthermore,

$$\lim_{t\to\infty} V_2(t) \leq \frac{\frac{1}{2}k_\mu c_1\Phi_{\max}^T\Phi_{\max} + \zeta_1^T\Phi_{\max}c_2}{k'}. \tag{75}$$

That is, $e(t)$, $\tilde{\Phi}(t)$ and $\varepsilon(t)$ converge to the residual set exponentially:

$$D = \left\{ e, \tilde{\Phi}, \varepsilon : \frac{1}{2}\frac{1}{b_{n-1}k_1}e^2 + \left(k_2 + \frac{1}{k_e b_{n-1}^2}\right)\varepsilon^T P\varepsilon + \frac{1}{2}\tilde{\Phi}^T\Gamma^{-1}\tilde{\Phi} < \frac{\frac{1}{2}k_\mu c_1 \Phi_{\max}^T \Phi_{\max} + \zeta_1^T \Phi_{\max} c_2}{k'} \right\}. \quad (76)$$

■

V. Illustrative Study and Applications

To verify the validity of the proposed OFRAC strategy, we fully test it in a virtual AM-AFM system [32]. Considering that the AFM system presents very complex dynamics and the phenomenon of sensor saturation usually badly degrades the imaging quality, we first compare the performance of the OFRAC strategy and the iterative learning control method [9]. After that, the strategy is employed in the virtual AM-AFM system to scan several types of samples, meanwhile, the currently utilized PI method is also utilized to image the same sample to provide some comparative study.

After considering the movement of the piezo-scanner in the Z direction and based on some experimental study for the hysteresis behavior, the following function is inserted to describe the hysteresis behavior of the piezo-scanner:

$$v(t) = \begin{cases} -0.000135u(t)^3 + 0.00374u(t)^2 + u(t) - 0.00358, \\ \dot{u}(t) \geq 0; \\ -0.0000711u(t)^3 - 0.00317u(t)^2 + u(t) + 0.00358, \\ \dot{u}(t) < 0, \end{cases} \quad (77)$$

where $u(t)$ is the input voltage of the piezo-scanner, while $v(t)$ represents the system output caused by hysteresis behavior of the piezo-scanner. Meanwhile, the following 3rd order model is used to describe the dynamics of the piezo-actuator:

$$G(s) = \frac{6.283 \times 10^4 s^2 + 1.935 \times 10^7 s + 1.168 \times 10^{13}}{s^3 + 6.306 \times 10^4 s^2 + 1.837 \times 10^8 s + 1.063 \times 10^{13}},$$

which indicates the input-output differential equation as:

$$\dddot{y}(t) + 6.306 \times 10^4 \ddot{y}(t) + 1.837 \times 10^8 \dot{y}(t) + 1.063 \times 10^{13} y(t) = 6.283 \times 10^4 \ddot{u}(t) + 1.935 \times 10^7 \dot{u}(t) + 1.168 \times 10^{13} u(t), \quad (78)$$

where $y(t)$ denotes the output of the system. After combing the dynamics (78) with the hysteresis behavior (77), the following improved model with hysteresis considered is obtained:

$$\dddot{y}(t) + 6.306 \times 10^4 \ddot{y}(t) + 1.837 \times 10^8 \dot{y}(t) + 1.063 \times 10^{13} y(t) = 6.283 \times 10^4 \ddot{v}(t) + 1.935 \times 10^7 \dot{v}(t) + 1.168 \times 10^{13} v(t)$$

$$v(t) = \begin{cases} -0.000135u(t)^3 + 0.00374u(t)^2 + u(t) - 0.00358, \\ \dot{u}(t) \geq 0; \\ -0.0000711u(t)^3 - 0.00317u(t)^2 + u(t) + 0.00358, \\ \dot{u}(t) < 0. \end{cases} \quad (79)$$

The high voltage amplifier and sensitivity are chosen as 16 and 9.7×10^{-9}nm/V. The cantilever with the quality factor of 40 is excited to oscillate with free amplitude of 30 nm around its natural frequency of 300 kHz. The other setup of the AM-AFM system can be referred to [32].

A. Comparative Study for the OFRAC Algorithm

Since the free oscillation amplitude of the cantilever is set as 30 nm, a sinusoidal sample with amplitude of 35 nm is utilized to make measurement saturation possible, the initial offset is chosen as 2 nm, the set-point is set as 0.2 V, while the resolution is chosen as 500 points per line.

To demonstrate the performance of the proposed OFRAC strategy, we implement comparative study with the recently developed iterative learning control law, since it is a typical high-speed AFM controller [9]. Two kinds of samples, a slowly-varying periodic sample and a dislocated sample, are selected for the comparison. When simulating the iterative learning control(ILC) algorithm, the real model of the system (79), denoted as G_{PD}, is utilized for the controller to achieve best tracking result. Subsequently, the inversion-based ILC filter is:

$$L = (G_{PD}S)^{-1},$$

where

$$S = (1 + G_{PD}G_{FB})^{-1}$$

is the sensitivity of the system, and G_{FB} denotes a H_∞ robust feedback controller. Meanwhile, the roll-off ILC filter Q is chosen to be one. The other parameters, such as scanning frequency and resolution, sampling time, and the plant parameters are all set the same for both ILC method and the proposed OFRAC strategy .

Results for a sinusoidal sample with slowly-varying period: We first test the performance of the designed OFRAC strategy with a sinusoidal sample, whose surface topography is expressed as:

$$d_i(t) = 35 \sin\left[2\pi(500 + 5i - 5)t\right]$$

where d_i is defined as the sample topography of the ith line.

Fig. 4 shows the comparison of control performance for the 100th scanning line between the proposed OFRAC method and the ILC approach, where the solid and dotted lines represent the results of the OFRAC strategy and the ILC method, respectively. No measurement noise is added to the system in Fig. 4 (a), while $\pm 2\%$ white noise relative to the setpoint is inserted into the laser detector in Fig. 4 (b). In the OFRAC strategy, the tracking error is only based on the current disturbance, and the system output is very close to the setpoint. However, for the ILC approach, as the tracking error is also related to that of the previous line, for such a sinusoidal sample with slowly-varying period, the performance is getting worse as time increases. From the previous results, it can be seen that the proposed OFRAC strategy exhibits much better response than the ILC method, which implies higher accuracy for the obtained images, especially for high-speed scanning tasks.

Results for a sinusoidal sample with dislocation: The sample topography in this case can be expressed as:

$$d_i(t) = 35 \sin\left(1000\pi t + \varphi\right)$$

where $\varphi = -\pi i/18$.

The obtained results are shown in Fig. 5. From these results, it can be seen that the proposed OFRAC controller makes the output converge to the setpoint with much less control error.

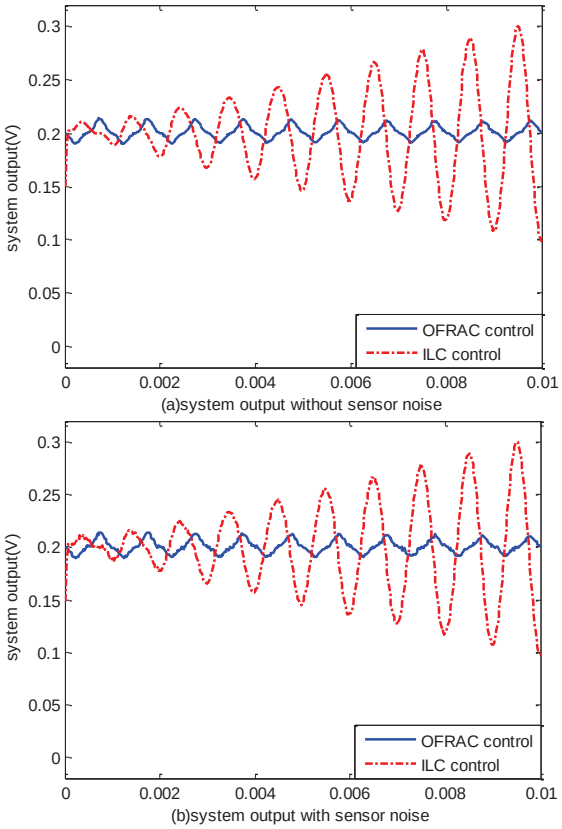

Fig. 4. Comparison of control perfomance for slowly-varying periodic sample (the 100th scanning line).

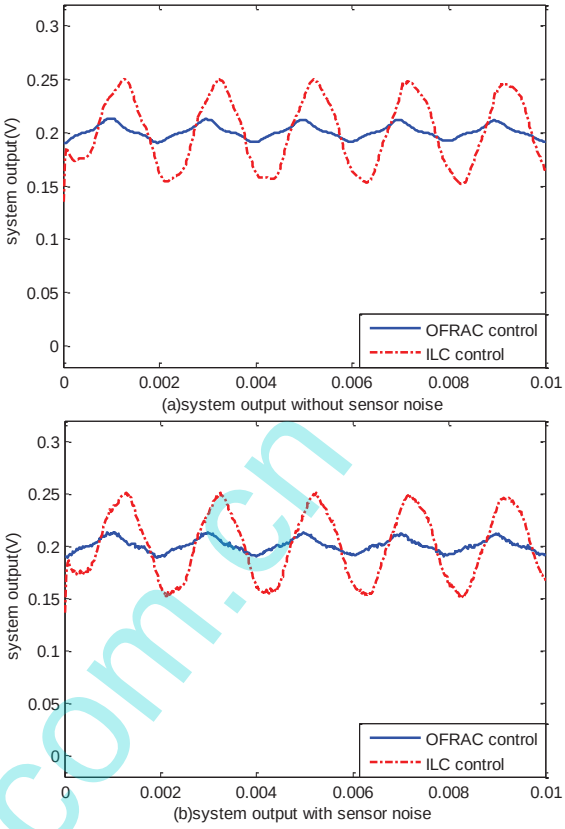

Fig. 5. Comparison of control perfomance for dislocated sample (the 100th scanning line).

B. Application and Analysis

To further compare the proposed OFRAC controller with the conventional PI controller, we implement both algorithms and employ them in the virual AM-AFM platform [32].

Scan of a Square Sample: To investigate the performance of the proposed controller, we first scan a square sample, whose image is shown in Fig. 6, under different frequencies of 10 Hz and 100 Hz, respectively.

When the scan frequency is low (for example, 1 Hz), both controllers can obtain accurate images for the sample. However, as the scan frequency increases, it becomes more and more difficult to obtain an image with high credibility, because the controller will then have less time for each scanning point. When the scan frequency is set as 10 Hz, the images of the sample are given in Fig. 7, with the top and bottom results obtained from the OFRAC controller and the PI controller, respectively. Apparently, the OFRAC-based method obtains a much more accurate image than the PI controller. To provide more specific analysis from the control theory standpoint, the control inputs of a single line for the two controllers are also provided in Fig. 8. From these curves, it can be seen that the input of the OFRAC controller follows very well with the topography of the sample, thus it yields a reliable image for the sample. However, the PI controller cannot track the edges of the sample (from the control standpoint, an edge can be regarded as a step-form signal exerted on the system), due to the reason that the PI controller needs much longer time

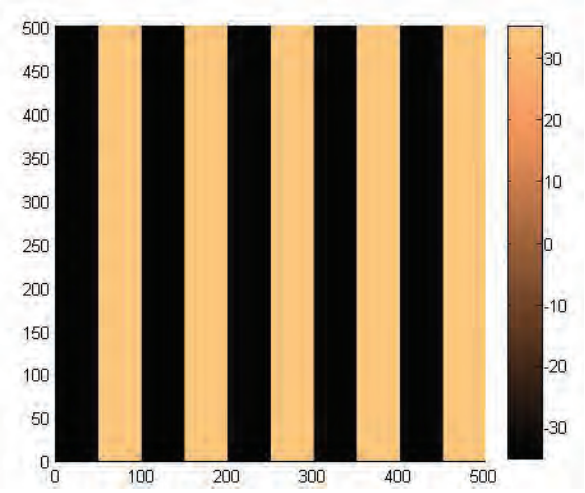

Fig. 6. A square sample.

to stabilize the system, therefore, when the scan frequency is sufficiently high, at the edging points, the system is still in the rising stage when the tip is moved to the next point.

To obtain more understanding for the OFRAC strategy, we increase the scan frequency to 100 Hz to image the sample. The obtained image is provided in Fig. 9, with results of both controllers included to facilitate comparison. It is easy to see that with the increasing of the scan frequency, the PI controller can no longer yield an accurate image for the sample due to

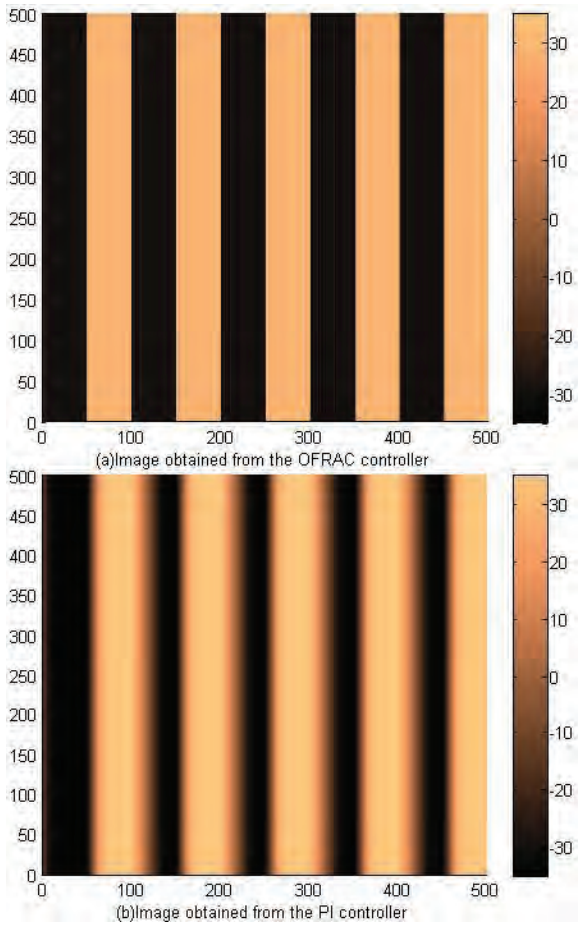

Fig. 7. Results of 10 Hz scan of a square sample.

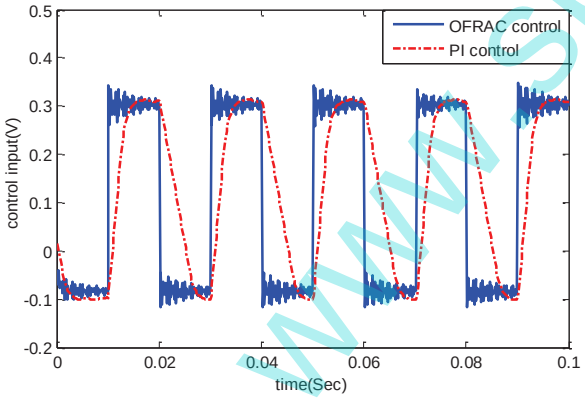

Fig. 8. Control inputs of a single line for 10 Hz scanning task.

the lower control bandwidth, yet the OFRAC controller still captures well with the topography of the sample.

Scan of Other Samples: We fully test the performance of the strategies with other samples, including sinusoidal samples, triangular samples, and so on. However, due to space limitation, only the scan results for a triangular sample, whose image is shown in Fig. 10, are included here to demonstrate the capacity of the proposed OFRAC strategy.

When the scan frequency is set high enough as 20 Hz, we

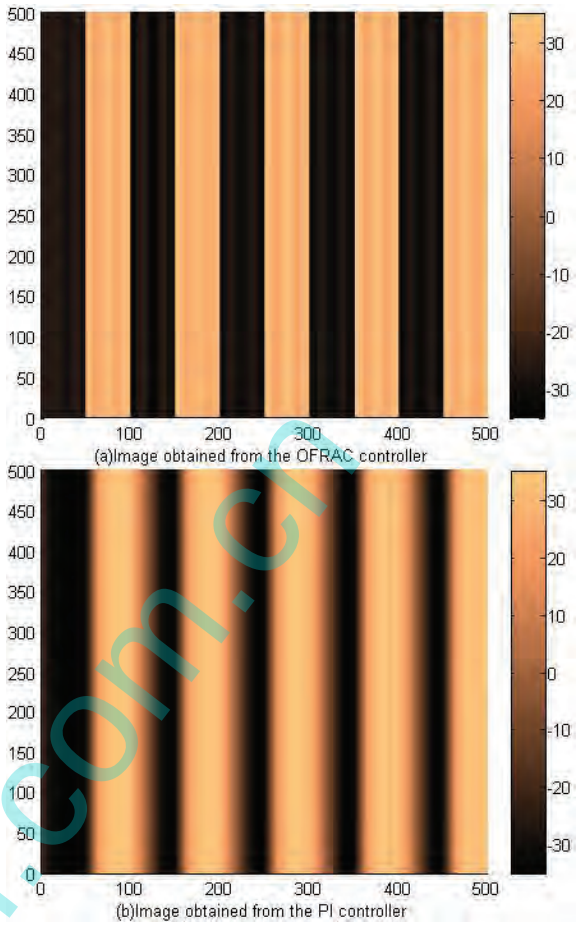

Fig. 9. Results of 100 Hz scan of a square sample.

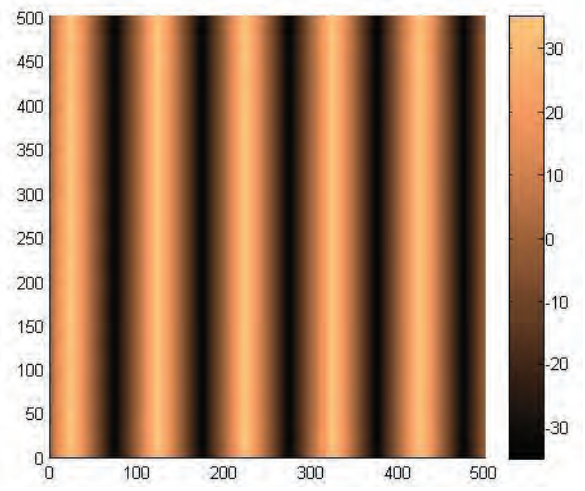

Fig. 10. A triangular sample.

employ the proposed OFRAC strategy and the conventional PI method to scan the triangular sample. The obtained results are provided in Fig. 11 for the system outputs, and Fig. 12 for the captured images of the sample. As demonstrated in Fig. 11, the output of the OFRAC strategy is much closer to the setpoint than that of the PI law. When comparing the resulting

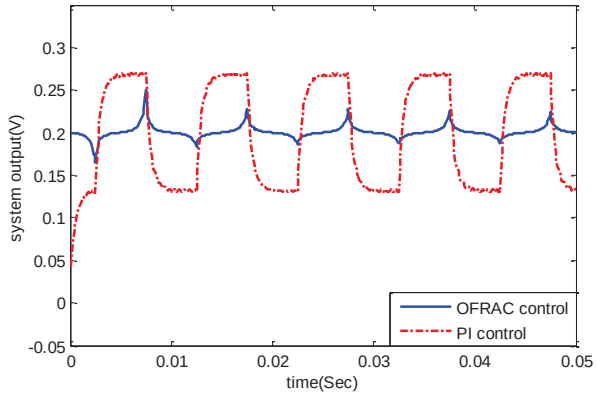

Fig. 11. Comparison of system outputs.

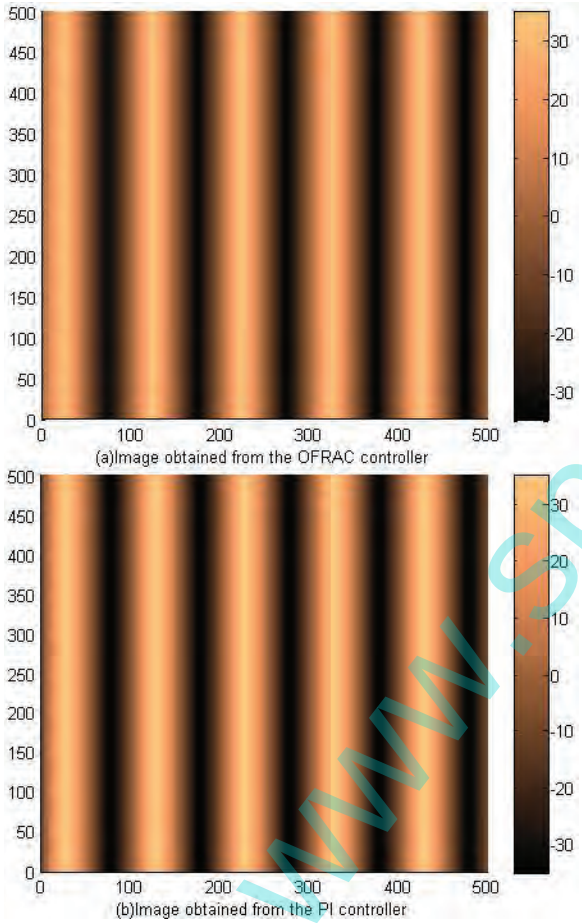

Fig. 12. Results of 20 Hz scan of a triangular sample.

images shown in Fig. 12 with Fig. 10, it can be seen that the OFRAC strategy yields an accurate image for the sample, yet the PI controller makes the peaks and valleys of the sample, respectively corresponding to the brightest and darkest zone in the image, appear much wider than they really are.

Remark 4: To apply the proposed OFRAC control strategy into a real-world AFM system, an AFM system with stable amplitude-modulation mode and open structure is needed to code and implement the control algorithm. For such an AFM system, a PI controller is often utilized to enable sample scanning. The application of the proposed OFRAC strategy mainly involves to code/test the algorithm, and then utilize it to take the place of the PI controller. Technically, the implementation of the proposed OFRAC strategy requires almost no additional conditions when compared with the original PI law, except that more computation and memory resource is needed to perform the calculation of the OFRAC algorithm, which is usually not a big issue since a high-performance Digital Signal Processor (DSP), or even a computer, is often utilized as the kernel control unit in an AFM system. However, to embed the proposed OFRAC strategy into a current AFM system, the system needs to present open structure, so as to enable input/output signals flow between the system and the coded OFRAC strategy.

VI. Conclusions

This paper first obtains a control-oriented model for an AM-AFM system, whose validity is supported by experimental results. Based on the obtained model, an OFRAC strategy is then designed to enhance the performance of the AM-AFM system. As proven by rigorous analysis, the OFRAC algorithm guarantees satisfactory performance even in the case of measurement saturation. The proposed modeling/control method is then employed in a virtual AM-AFM system, and numerous scan results for various samples are collected to show that the designed method exhibits superior performance over the currently utilized strategies.

In the future work, this algorithm will be used on a dynamic AFM to improve its imaging performance. Furthermore, some filtering techniques will be proposed to utilize the dynamic output of the piezo-scanner, intead of the control signal, to obtain a more accurate image. Besides, the convergence of the self-adaptive parameters will also be analyzed to enhance the system performance. To further increase the positioning accuracy, our future effort will also target to compensate for the hysteresis of the piezo-scanner by combining the proposed OFRAC strategy with some latest research results on hysteresis compensation.

References

[1] Bining G, Quate C, Gerber C, “Atomic Force Microscopy”, *Physical Review Letters*, Vol. 56, No. 9, pp. 930-933, 1986.

[2] M. Shibata, H. Yamashita, T. Uchihashi, H. Kandori, and T. Ando, “High-speed atomic force microscopy shows dynamic molecular processes in photo-activated bacteriorhodopsin”, *Nature Nanotechnology*, 2010(5): 208-212.

[3] Shigeto Inoue, Takayuki Uchihashi, Daisuke Yamamoto and Toshio Ando, “Direct observation of surfactant aggregate behavior on a mica surface using high-speed atomic force microscopy”, *Chem. Commun.*, 2011(47): 4974-4976.

[4] C. D. Onal, O. Ozcan, and M. Sitti, “Automated 2-D Nanoparticle Manipulation Using Atomic Force Microscopy”, *IEEE Transactions on Nanotechnology*, 2011, 10(3): 472-481.

[5] Q. Zhong, D. Inniss, K. Kjoller and V. B. Elings, “Fractured Polymer/Silica Fiber Surface Studied by Tapping Mode Atomic Force Microscopy”, *Surface Science Letters*, Vol. 290, No. 1-2, pp. L688-L692, June, 1993.

[6] Michele Basso, Paolo Paoletti, Bruno Tiribilli, and Massimo Vassalli, “AFM Imaging via Nonlinear Control of Self-Driven Cantilever Oscillations”, *IEEE Transactions on Nanotechnology*, 2011, 10(3): 560-565.

[7] A. J. Fleming, "Dual-Stage Vertical Feedback for High-Speed Scanning Probe Microscopy", *IEEE Transactions on Control Systems Technology*, 2011, 19(1): 156-165.
[8] S. Necipoglu, S. A. Cebeci, Y. E. Has, L. Guvenc, and C. Basdogan, "Robust Repetitive Controller for Fast AFM Imaging", *IEEE Transactions on Nanotechnology*, 2011, 10(5): 1074-1082.
[9] Y. Wu, Q. Zou, C. Su, "A Current Cycle Feedback Iterative Learning Control Approach for AFM Imaging", *IEEE Transactions on Nanotechnology*, 2009, 8(4): 515-527.
[10] Ricardo García, Rubén Pérez, "Dynamic Atomic Force Microscopy methods", *Surface Science Reports*, Vol. 47, pp. 197-301, 2002.
[11] Abu Sebastian, Anil gannepalli, and Murti V. Salapaka, "A Review of the Systems Approach to the Analysis of Dynamic-Mode Atomic Force Microscopy", *IEEE Trans. Control Systems Technology*, Vol. 15, No. 5, pp. 952-959, Sep. 2007.
[12] Deepak R. Sahoo, Abu Sebastian and Murti V. Salapaka, "Harnessing the Transient Signals in Atomic Force Microscopy", *Int. J. Robust Nonlinear Control*, Vol. 15, No. 16, pp. 805-820, 2005.
[13] Yudong Zhang, Yongchun Fang, Jie Yu, and Xiaokun Dong, "Note: A Novel Atomic Force Microscope Fast Imaging Approach: Variable-Speed Scanning", *Review of Scientific Instrument*, 82, 056103 (2011).
[14] Osamah M. EI Rifai, and Kamal Youcef–Toumi, "On Automating atomic force microscopes: An Adaptive Control Approach", *Control Engineering Practice*, Vol. 15, No. 3, pp. 349-361, March, 2007.
[15] Xianwei Zhou, Xiaokun Dong, Yudong Zhang, Yongchun Fang, "Automatic Tuning of PI Controller for Atomic Force Microscope Based on Relay with Hysteresis", *Proc. of the IEEE Conference on Control Applications*, Saint Petersburg, Russia, pp. 1271-1275, July 2009.
[16] Changyun Wen, Jing Zhou, Zhitao Liu, and Hongye Su, "Robust Adaptive Control of Uncertain Nonlinear Systems in the Presence of Input Saturation and External Disturbance", *IEEE Transactions on Automatic Control*, 2011, 56(7): 1672-1678.
[17] T. J. Zhang, G. Feng, H. P. Liu, and J. H. Lu, "Piecewise Fuzzy Anti-Windup Dynamic Output Feedback Control of Nonlinear Processes with Amplitude and Rate Actuator Saturation", *IEEE Transactions on Automatic Control*, 2009, 17(2): 253-264.
[18] Santosh Devasia, Evangelos Eleftheriou, and S. O. Reza Moheimani, "A Survey of Control Issues in Nanopositioning", *IEEE Trans. Control Systems Technology*, Vol. 15, No. 5, pp. 802-823, Sep. 2007.
[19] Yongchun Fang, Xiao Ren, Yudong Zhang, "Positioning Control Strategy Design for AFM Based Nanomanipulation Systems", *Proc. of 2011 International Conference on Advanced Mechatronic Systems*, Zhengzhou, China, Aug. 2011, pp. 461-465.
[20] Yudong Zhang, Yongchun Fang, Xianwei Zhou, Xiaokun Dong, "Image-Based Hysteresis Modeling and Compensation for an AFM Piezo-Scanner", *Asian Journal of Control*, Vol. 11, No. 2, pp. 166-174, 2009.
[21] Qinmin Yang, S. Jagannathan, and E. W. Bohannan, "Automatic drift compensation using phase-correlation method for nanomanipulation", *IEEE Transaction on Nanotechnology*, Vol. 7, no.2, pp. 209-216, 2008.
[22] Xinkai Chen, Toshikuni Ozaki, "Adaptive Control for Plants in the Presence of Actuator and Sensor Uncertain Hysteresis", *IEEE Transactions on Automatic Control*, Vol. 56, No. 1, pp. 171-177, 2011.
[23] Georg Schitter, Karl J. Åström, Barry E. Demartini, Philipp J. Thurner, Kimberly L. Turber, and Paul K. Hansma, "Design and Modeling of a High-Speed AFM-Scanner", *IEEE Trans. Control Systems Technology*, Vol. 15, No. 5, pp. 906-915, Sep. 2007.
[24] Xianwei Zhou, Yongchun Fang, Xiaokun Dong, and Yudong Zhang, "System Modeling of an AFM System in Z-axis", *Proc. Intl. Conf. Nanotechnology*, Hong Kong, China, pp. 96-99, Aug. 2007.
[25] Pranav Agarwal, Tathagata De, and Murti V. Salapaka, "Real Time Reduction of Probe-loss Using Switching Gain Controller for High Speed Atomic Force Microscopy", *Review of Scientific Instruments*, Vol. 80, No. 10, p. 103701, Oct. 2009.
[26] Maugis D., "Adhesion of spheres:The JKR-DMT transition using a dugdale model", *Journal of Colloid and Interface Science*, Vol. 150, pp. 243-269, Apr. 1992.
[27] Álvaro San Paulo, and Ricardo García, "Tip-Surface Forces, Amplitude, and Energy Dissipation in Amplitude-Modulation (Tapping Mode) Force Microscopy", *Physical Review B*, Vol. 64, No. 19, p. 193411, Nov. 2001.
[28] Hendrik Hölscher, Udo D. Schwarz, "Theory of Amplitude Modulation Atomic Force Microscopy with and without Q-Control", *International Journal of Non-Linear Mechanics*, Vol. 42, pp. 608-625, 2007.
[29] H. K. Lam, "Stabilization of Nonlinear Systems Using Sampled-Data Output-Feedback Fuzzy Controller Based on Polynomial-Fuzzy-Model-Based Control Approach", *IEEE Transactions on Systems, Man, and Cybernetics, Part B*, Vol. 42, No. 1, pp. 258-267, 2012.
[30] Krstic M., Kanellakopoulos I., and Kokotovic P. V., *Nonlinear and Adaptive Control Design*, New York: Wiley, 1995.
[31] Jian-Xin Xu, Tong-Heng Lee and Qing-Wei Jia, "An Adaptive Robust Control Scheme for a Class of Nonlinear Uncertain Systems", *International Journal of Systems Science*, Vol. 28, No. 4, pp. 429-434, 1997.
[32] Xianwei Zhou, Yongchun Fang, "A Virtual Tapping-Mode Atomic Force Microscope", in *Proc. 1st IEEE International Conf. Nano/Micro Engineered and Molecular Systems*, pp. 501-504, Zhuhai, China, Jan. 2006.

Yongchun Fang (S'00−M'02−SM'08) received the B.S. degree in electrical engineering and the M.S. degree in control theory and applications from Zhejiang University, Hangzhou, China, in 1996 and 1999, respectively, and the Ph.D. degree in electrical engineering from Clemson University, Clemson, SC, in 2002.

From 2002 to 2003, he was a Postdoctoral Fellow with the Sibley School of Mechanical and Aerospace Engineering, Cornell University, Ithaca, NY. He is currently a Professor with the Institute of Robotics and Automatic Information System (IRAIS), Nankai University, Tianjin, China. His research interests include AFM-based Nano-systems, visual servoing, and control of underactuated systems including overhead cranes.

Yudong Zhang received the B.S. degree in automation from Nankai University, Tianjin, China, in 2006, and the Ph.D. degree in control theory and control engineering at the Institute of Robotics and Automatic Information System (IRAIS), Nankai University, in 2011.

His research interests include AFM-based nanorobotics, nano-system control and nonlinear control.

Ningning Qi received the B.S. degree in automation from Nankai University, Tianjin, China, in 2008. She is currently working toward the M.S. degree in the Institute of Robotics and Automatic Information System, Nankai University, Tianjin.

Her research interests include nanopositioning and adaptive control of atomic force microscopes.

Xiaokun Dong received the B.S. degree in automation from Tianjin University, Tianjin, China, in 2005. And he received the Ph.D. degree in the Institute of Robotics and Automatic Information System, Nankai University, Tianjin, in 2012.

His research interests include AFM imaging method and AFM-based nano-manipulation.